Ultrahigh photosensitivity and detectivity of hydrogen-treated TiO_2 nanorod array/SiO_2/Si heterojunction broadband photodetectors and its mechanism

Ling, C. C.; Guo, T. C.; Lu, W. B.; Li, X. F.; Zhu, L.; Ma, M.; Xue, Q. Z.

DOI
10.1039/c7tc05580c

Publication date
2018

Document Version
Final published version

Published in
Journal of Materials Chemistry C

Journal of Materials Chemistry C

PAPER

View Article Online
View Journal | View Issue

Cite this: J. Mater. Chem. C, 2018, 6, 2319

Ultrahigh photosensitivity and detectivity of hydrogen-treated TiO_2 nanorod array/SiO_2/Si heterojunction broadband photodetectors and its mechanism†

C. C. Ling,[ab] T. C. Guo,[b] W. B. Lu,[b] X. F. Li,[b] L. Zhu,[ab] M. Ma*[c] and Q. Z. Xue *[ab]

Received 5th December 2017,
Accepted 31st January 2018

DOI: 10.1039/c7tc05580c

rsc.li/materials-c

It is demonstrated that hydrogen treatment as a simple, effective strategy can greatly improve the broadband photo-responsive performance of pristine TiO_2 nanorod arrays (NRAs)/SiO_2/n-Si heterojunctions. The hydrogen-treated TiO_2 NRAs/SiO_2/n-Si heterojunction shows a stable, repeatable and broadband photo response from 365 nm to 980 nm at 100 μW cm^{-2}. The responsivity (R) of H:TiO_2 NRAs/SiO_2/n-Si approaches the ultrahigh value of 468 A W^{-1} and it has an outstanding detectivity (D^*) of 1.96 × 10^{14} cm $Hz^{1/2}$ W^{-1} and an excellent sensitivity (S) of 2.63 × 10^7 cm^2 W^{-1}, in contrast to the values of R (10^{-6}–10^{-1} A W^{-1}) or S (2 × 10^3 cm^2 W^{-1}) from reported TiO_2 nanofilm/TiO_2 NRAs/n-Si(111) photodetectors, indicating a huge responsivity enhancement of up to 4–8 orders of magnitude. Additionally, the response and recovery time are extremely short (3.5–3.9 ms). The comprehensive characteristics make the device stand out among the previously reported 1D metal oxide nanostructure/Si based photodetectors. In fact, the R, S and D^* values of the heterojunction are 2–4 orders of magnitude higher than those of some new 2D nanomaterials/Si based photodetectors. The excellent photo-responsive performance may be attributed to the energy band structure of the TiO_2@$TiO_{2-x}H_x$ core/shell structure, the interface effect of the TiO_2@$TiO_{2-x}H_x$/Si heterojunction, *etc.* This research provides a new concept for the design of other metal oxide based heterojunction photodetectors.

1. Introduction

Broadband photodetectors (PDs) with a broad spectral response from the ultraviolet (UV) to the visible to the near infrared (NIR) light regions have attracted great attention in a variety of industrial and scientific applications, including image sensing, communication, environmental monitoring and day and night time surveillance.[1–9]

Recently, due to easy CMOS-compatible processing and reduced cost, Si-based heterojunction broadband detectors, including metal oxide 1D nanostructure/Si heterojunctions and new 2D nanomaterials/Si heterojunctions, *etc.*, have become highly desirable. They are mainly composed of Schottky diodes,[10,11] p–n or n–n heterojunctions[12,13] and metal–semiconductor–metal (MSM) junctions.[14,15] Additionally, it has been demonstrated that p–n or n–n heterojunction photo-detectors show superior photo response properties[16,17] to those of other types of PDs.[18–20] For example, metal oxide 1D nanostructure/Si heterojunctions, such as ZnO nanorod/Si (lateral structure) heterojunctions,[21] ZnO nanowire array/n-Si(100) (vertical structure) heterojunctions[22] and ZnO nanorod array/SiO_2/p-Si heterojunctions,[23] have been investigated widely. These heterojunctions can detect UV-visible light[22] by varying the bias polarity or at a high voltage value (15 V).[23] In addition, it has been demonstrated that TiO_2 nanofilm/TiO_2 NRAs/n-Si(111) (vertical structure) PDs show multi-colored photo response characteristics for UV or VIS light upon varying the bias value, but the on–off ratio of the PDs is only ~2 at 1 mW cm^{-2} and the responsivity (R) and sensitivity (S) of the PDs are extremely low and are 10^{-6}–10^{-1} A W^{-1} and ~2 × 10^3 cm^2 W^{-1},[24] respectively. In comparison with one-dimensional metal oxide/Si heterojunction materials, new 2D nanomaterial/Si heterojunctions have demonstrated better photo-responsive characteristics. For example, the R, S and detectivity (D^*) of Bi_2Se_3/Si,[25] WS_2/Si,[18] In_2Te_3/Si,[17] NiSe/Si,[26] $SnSe_2$/Si,[27] In_2S_3/Si,[28] *etc.*, are 10^{-2}–10^2 A W^{-1}, ~10^5 cm^2 W^{-1} and 10^9–10^{12} cm $H^{1/2}$ W^{-1}, respectively.

It has been demonstrated that annealing the TiO_2 nanostructure in a reducing gas H_2 atmosphere can increase the

[a] State Key Laboratory of Heavy Oil Processing, China University of Petroleum, Qingdao 266580, Shandong, P. R. China. E-mail: xueqingzhong@tsinghua.org.cn
[b] College of Science, China University of Petroleum, Qingdao 266580, Shandong, P. R. China
[c] Materials for Energy Conversion and Storage (MECS), Department of Chemical Engineering, Delft University of Technology, Van der Maasweg 9, 2629 HZ Delft, The Netherlands. E-mail: m.ma-1@tudelft.nl

† Electronic supplementary information (ESI) available. See DOI: 10.1039/c7tc05580c

density of oxygen vacancies[29,30] and form a unique crystalline core–amorphous shell (TiO_2@$TiO_{2-x}H_x$) structure[31–34] which can greatly enhance its broad spectral response.[35–37] Meanwhile, the TiO_2@$TiO_{2-x}H_x$ structure plays a critical role in determining the Fermi level of H_2-treated TiO_2 (H:TiO_2),[35–37] which can modulate the minority carriers in H:TiO_2. In addition, it is well known that at reverse voltage the minority carriers of p–n or n–n heterojunction photodetectors can change a lot from under darkness to under illumination, which can be the working basis for p–n or n–n heterojunction photodetectors.[24] Herein we demonstrated that H_2-treatment is a simple and effective method to improve the broadband photo-responsive performance of a pristine TiO_2 NRAs/SiO_2/n-Si heterojunction. It is found that the S and detectivity (D^*) of TiO_2 NRAs/SiO_2/n-Si can be enhanced by 2–4 orders of magnitude by H_2-treatment. More importantly, the comprehensive characteristics of this heterojunction make the device stand out among the previously reported 1D metal oxide nanostructure/Si based photodetectors. In particular, the R of H:TiO_2 NRAs/SiO_2/n-Si approaches the ultrahigh value of 468 A W^{-1} with an outstanding D^* of $\sim 1.96 \times 10^{14}$ cm $H^{1/2}$ W^{-1} and an excellent S of $\sim 2.63 \times 10^7$ cm^2 W^{-1}, in contrast to the value of R (10^{-6}–10^{-1} A W^{-1}) or S ($\sim 2 \times 10^3$ cm^2 W^{-1}) for the photodetector based on TiO_2 nanofilm/TiO_2 NRAs/n-Si(111),[24] indicating a huge responsivity enhancement of up to 4–8 orders of magnitude. In fact, the R, S and D^* of the heterojunction are 2–4 orders of magnitude higher than those of some new 2D nanomaterial/Si heterojunctions. Consequently, practical ultrahigh photo-responsive performance broadband PDs may be achieved in the future.

2. Results and discussion

2.1 Synthesis and characterization of H:TiO_2 NRAs

Fig. 1 shows the schematic illustration of the fabrication process to integrate H:TiO_2 NRAs on an n-Si wafer. As shown in Fig. 1a, the TiO_2 seed layer was fabricated on the n-type Si and the 1.2 nm thick SiO_2 native oxide layer was reserved on the surface of the Si.[38] TiO_2 NRAs were then grown on the Si wafer using the hydrothermal method in Fig. 1b. As shown in Fig. 1c, the TiO_2 NRAs on Si were annealed in a pure hydrogen atmosphere for 60 min at various temperatures in the range 350–500 °C, and developed into H:TiO_2 NRAs. The morphologies of the H:TiO_2 NRAs were determined by using a JEOL JSM-6500 field emission SEM. As shown in the front-view and cross-sectional SEM images in Fig. 2a, it is demonstrated that the H:TiO_2 NRAs grow densely on the Si substrate with a length of ~ 1 μm and a diameter of ~ 50 nm. From the energy dispersive X-ray spectroscopy (EDS) mapping of a H:TiO_2 nanorod in Fig. 2b and c, we can directly observe a uniform distribution of Ti and O elements. As shown in Fig. 2d, the high-magnification TEM image of the H:TiO_2 nanorods shows that the H:TiO_2 nanorods have a disordered amorphous layer of $TiO_{2-x}H_x$ (1–2 nm) surrounding a crystalline core to form an crystalline core/amorphous shell TiO_2@$TiO_{2-x}H_x$ structure. Moreover, from the EDS spectrum shown in Fig. 2e, the Ti and O signals can be easily detected and show a non-stoichiometric atomic ratio of Ti and O (~ 1.1), demonstrating again that the structure of H:TiO_2 is defective. In order to prevent the H:TiO_2 NRAs from being oxidized, a layer of transparent conducting Pd thin film, which is difficult to oxidize, was deposited on the surface of the H:TiO_2 NRAs/SiO_2/n-Si heterojunction from a Pd target using DC magnetron sputtering.

X-ray photoelectron spectroscopy (XPS) is a powerful tool to investigate the change of surface chemical bonding as well as the electronic valence band position, as shown in Fig. 3a and b. The Ti 2p XPS spectra were almost identical for TiO_2 and H:TiO_2 with the Ti $2p_{3/2}$ and Ti $2p_{1/2}$ peaks centered at binding energies of 458.2 and 464.1 eV, which are typical for the Ti^{4+}–O bonds in TiO_2.[30,31,33] The O 1s XPS spectra of the two samples show some differences in Fig. 3b. The single O 1s peak at 529.6 eV for TiO_2 and H:TiO_2 is typically assigned to Ti–O bonds. The broader O 1s peak for H:TiO_2 at about 531.8 eV is due to

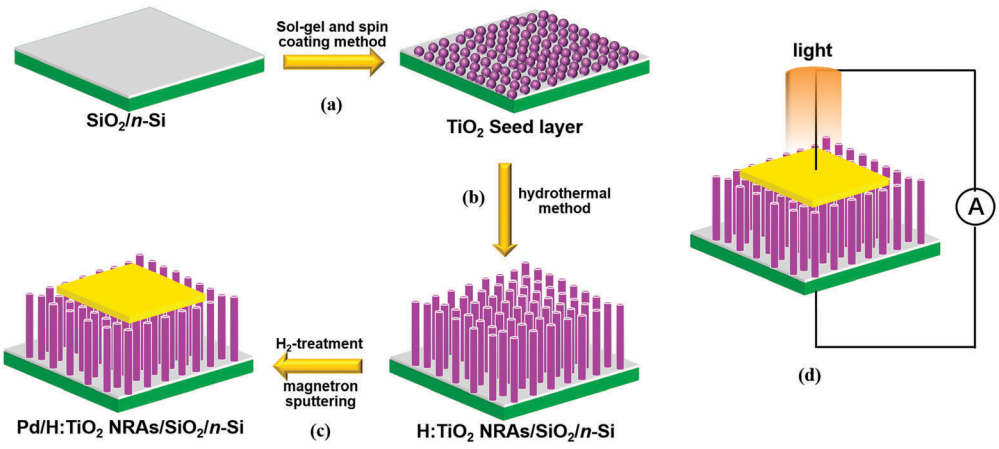

Fig. 1 Schematic illustration of the fabrication process to integrate H:TiO_2 NRAs on an n-Si wafer. (a) The nano-size TiO_2 seed layer was planted on the n-Si surface using a sol–gel and spin coating method. (b) TiO_2 NRAs grew from the seeds *via* a hydrothermal process. (c) H:TiO_2 NRAs were produced through H_2-treating TiO_2 NRAs and a transparent Pd conductive layer was deposited on the surface of the H:TiO_2 NRAs, which served as a top electrode. (d) Schematic illustration of the H:TiO_2 NRAs/SiO_2/Si heterojunction photodetector.

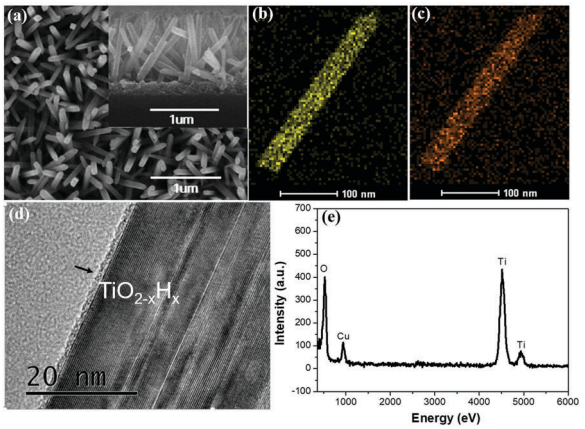

Fig. 2 (a) Front-view SEM image of H:TiO_2 NRAs (inset is a cross sectional SEM image of the H:TiO_2 NRAs). (b) Ti and (c) O elemental mapping of a H:TiO_2 nanorod. (d) High-magnification TEM image of a H:TiO_2 nanorod. (e) EDS spectrum of a H:TiO_2 nanorod.

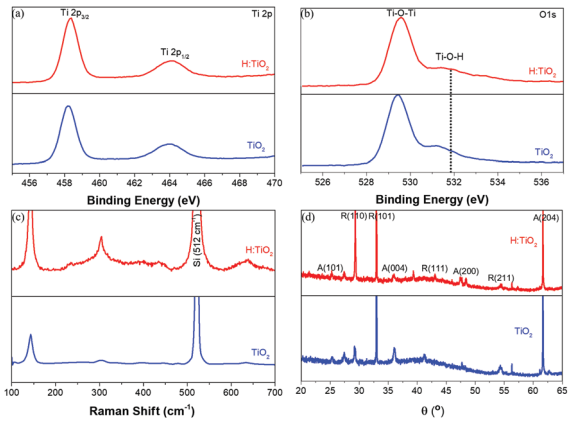

Fig. 3 (a) Ti 2p and (b) O 1s XPS spectra for TiO_2 and H:TiO_2. (c) Raman spectra of TiO_2 and H:TiO_2 and (d) XRD patterns for TiO_2 and H:TiO_2.

Ti–O–H bonds in $TiO_{2-x}H_x$.[30,31] The data confirm the formation of hydroxyl groups on the TiO_2 surface after H_2-treatment.

The structural properties of TiO_2 and H:TiO_2 NRAs were further examined by measuring Raman scattering. For the H:TiO_2 NRAs, five peaks at 144 cm^{-1}, 225 cm^{-1}, 300 cm^{-1}, 440 cm^{-1} and 615 cm^{-1} can be observed. The peaks of the H:TiO_2 NRA samples at 144 cm^{-1}, 225 cm^{-1}, 300 cm^{-1}, 440 cm^{-1} and 615 cm^{-1} match well with the peaks of the TiO_2 NRAs. In addition, the results show that oxygen vacancies defects and impurities cause these peaks to broaden and shift.[31,32] X-ray diffraction (XRD) patterns of the TiO_2 and H:TiO_2 NRAs are shown in Fig. 3d. The diffraction peaks of the TiO_2 and H:TiO_2 NRAs are hardly distinguishable, there is no phase change after hydrogenation, and the peaks are well-indexed to the rutile structure of TiO_2 (cassiterite, JCPDS No. 41-1445), indicating the degree of crystallinity. The diffraction peaks observed at 25.9°, 29.3°, 32.5°, 36.1°, 41.0°, 42.5°, 54.0° and 62.0° can be assigned to the anatase (A) (101), rutile (R) (110), R (101), A (004), R (111), A (200), R (211) and A (204) planes of TiO_2, respectively.

2.2 The effect of hydrogenation on the photo response of the H:TiO_2 NRAs/SiO_2/Si heterojunction

Fig. 1d demonstrates the schematic illustration of the H:TiO_2 NRAs/SiO_2/Si heterojunction photodetector, and the monochromatic light is vertically incident on the surface of the H:TiO_2 NRAs in order to measure its photo-responsive properties. The electrodes on the Pd film surface and the opposite Si surface of the H:TiO_2 NRAs/SiO_2/n-Si broadband detector were made using In solder. As noted, there are 4 junctions in the In/Pd/H:TiO_2 NRAs/SiO_2/Si/In device, including the Si/In, Pd/TiO_2, In/Pd and TiO_2 NRAs/SiO_2/Si junctions.[24] It was demonstrated that the contact between the metal and Si hardly affected the detection performance of the device at a certain reverse bias (for the heterojunction). There is a good Ohmic contact between the TiO_2 and the Pd electrode with no interfacial barrier or traps.[24] In addition, it is well known that the contact between metal and metal is an Ohmic contact. Therefore, the Si/In, Pd/TiO_2 and In/Pd junctions have little influence on the *I–V* characteristics of the H:TiO_2 NRAs/SiO_2/n-Si heterojunction. Additionally, the *I–V* characteristics of the In/Pd/H:TiO_2 NRAs/SiO_2/Si/In structure should be determined by the H:TiO_2 NRAs/SiO_2/n-Si heterojunction. To keep the same bias voltage polarity, a forward bias voltage was applied to the H:TiO_2 NRAs and conversely, a reverse bias voltage was applied to n-Si.

In order to investigate the influence of H_2 treatment on the photo response of the TiO_2 NRAs/SiO_2/Si heterojunctions, we investigated the photo-responsive properties of the TiO_2 NRAs/SiO_2/Si (fabricated) heterojunction and the H:TiO_2 NRAs/SiO_2/Si heterojunction annealed at 350 °C or 500 °C, at a reverse voltage of 7 V under darkness and 950 nm light, as shown in Fig. 4. As shown in Fig. 4a, the *I–V* characteristics of the TiO_2 NRAs/SiO_2/Si and H:TiO_2 NRAs/SiO_2/Si heterojunctions are measured under darkness or under 950 nm light of 100 μW cm^{-2}. The *I–V* curves of the device show the good rectifying behavior of the heterojunction. It is demonstrated that the heterojunctions show the characteristics of a diode which can be described using

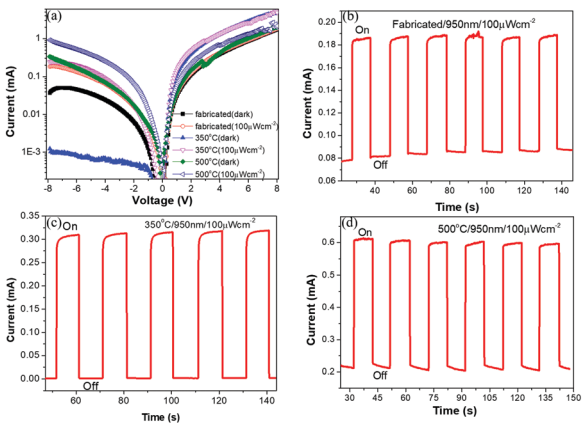

Fig. 4 (a) The *I–V* curves of TiO_2 NRAs/SiO_2/Si (fabricated) and H:TiO_2 NRAs/SiO_2/Si with H_2-treatment at 350 °C or 500 °C under darkness and 950 nm light. (b–d) Photocurrent *versus* time plots of TiO_2 NRAs/SiO_2/Si (fabricated) and H:TiO_2 NRAs/SiO_2/Si with H_2-treatment at 350 °C or 500 °C at −7 V.

thermionic emission theory in which the *I–V* relationship is given by $I = I_0 \exp[(qV/nkT) - 1]$, where q is the electronic charge, V is the applied voltage, k is the Boltzmann constant, n is the ideality factor and I_0 is the reverse saturation current, which is given by $I_0 = AA^{\star}T^2 \exp(-q\,\phi_B/kT)$, where A is the effective area of the heterojunction contact, $A^{\star}$ is the Richardson constant and ϕ_B is the barrier height of the heterojunction. The ideality factor of a diode is a measure of how closely it follows ideal behavior on a logarithmic scale and has a value of unity in the ideal case. It was found that there are almost no differences between the photocurrent and the dark current at forward bias. However, at reverse bias the photocurrent demonstrated an obvious difference from the dark current. It is demonstrated that the reverse *I–V* characteristics of the H:TiO_2 NRAs/SiO_2/Si heterojunction showed potential for good photo-detection performance, which is the basis for PDs. Fig. 4b–d show photocurrent *versus* time plots for the TiO_2 NRAs/SiO_2/Si heterojunction and the H:TiO_2 NRAs/SiO_2/Si heterojunction annealed at 350 °C or 500 °C, under 950 nm light. By analyzing these data, it can be shown that with an increase in annealing temperature the dark currents change greatly, first decreasing and then increasing, and the dark currents are 8.72×10^{-5} A, 7.2×10^{-7} A and 2.1×10^{-4} A for the fabricated sample and the samples annealed at 350 °C and 500 °C, respectively, showing that the dark current reached the lowest value at 350 °C and is reduced by 2 orders of magnitude. In addition, it is shown that with increasing temperature the photocurrents are 1.88×10^{-4} A, 3.0×10^{-4} A and 6.23×10^{-4} A, respectively, and increase about 3 times.

R, *D** and *S* are usually used to describe the photo-responsive properties of PDs.[39] *R* is defined as the photocurrent generated per unit power of the incident light on the effective area. It is calculated according to the following equation: $R = I_p/PA$, where P and A are the incident power density and the active area, respectively. $D^{\star}$ represents the ability of a PD to detect weak optical signals, and can be calculated according to the following equation: $D^{\star} = A^{1/2}R/(2qI_{dark})^{1/2}$, where q and I_d are the elementary charge and the dark current, respectively. Considering that the photo-to-dark current ratio is dependent on the incident light power density, when describing the photo switching behavior *S* should be defined as the photo-to-current ratio per unit power. *S* can be expressed as $S = I_p/I_{dark}P$. As shown in Fig. S1 (ESI†), the *S*, *D** and *R* values of TiO_2 NRAs/SiO_2/Si and H:TiO_2 NRAs/SiO_2/Si under 950 nm light at −7 V can demonstrate the effect of the H_2 treatment temperature on the photo-responsive properties of heterojunctions. H:TiO_2 NRAs/SiO_2/Si possesses excellent photo-responsive characteristics annealed with H_2 at 350 °C. Three figure-of-merits of H:TiO_2 NRAs/SiO_2/Si show high values, and *S*, *D** and *R* are estimated to be 8.7×10^5 cm^2 W^{-1}, 5.56×10^{12} cm Hz$^{1/2}$ W^{-1} and 11.4 A W^{-1}, respectively, at 350 °C. The results reveal that the introduced oxygen vacancies can significantly enhance the photoresponsive performance of H:TiO_2 NRAs/SiO_2/Si heterojunctions.[40,41] However, it is worth noting that at 500 °C the dark current is equivalent to the photocurrent and the photo-responsive performance of H:TiO_2 NRAs/SiO_2/Si is reduced. Fig. S2 (ESI†) shows XRD spectra of H:TiO_2 nanowires annealed in hydrogen at various temperatures (350 and 500 °C). The strong characteristic peaks of H:TiO_2 gradually reduce or disappear and a group of new peaks corresponding to Ti metal emerge when the hydrogen treatment temperature is higher (500 °C). This indicates that hydrogen treatment at high temperature damaged the H:TiO_2 nanorods by reducing TiO_2 to Ti metal.[42] The excess of oxygen vacancies causes the H:TiO_2 NRAs/SiO_2/Si heterojunctions to change into Ti/SiO_2/Si (metal–semiconductor) heterojunctions[39] and the dark current became larger, which may hinder further improvement of the photoresponsive performance.[40] Based on the above discussion, it is confirmed that hydrogen treatment at a suitable temperature is important for making TiO_2 NRAs/SiO_2/Si achieve ultrahigh photo-responsive properties.[40]

2.3 Broadband photo response of the H:TiO_2 NRAs/SiO_2/Si heterojunction

In order to comprehensively show the photo-responsive properties of the H:TiO_2 NRAs/SiO_2/Si heterojunctions, the *I–V* curves of the heterojunction under 900 nm light of 0.5 μW cm^{-2}, 2 μW cm^{-2}, 10 μW cm^{-2}, 30 μW cm^{-2} and 100 μW cm^{-2} are shown in Fig. 5a. It is found that the photocurrent increases gradually at reverse voltage with increasing light power density. Additionally, with an increasing voltage value the photocurrent increases and finally reaches saturation after −7 V. The saturation voltage (−7 V) of the photocurrent is basically stable with increasing light power intensity. Furthermore, we evaluated the photocurrent switching behavior of the H:TiO_2 NRAs/SiO_2/Si heterojunction photodetector. The temporal responses of the photodetector measured at different bias voltages and light power densities, as shown in Fig. 5b and f, show that the device could be reversibly switched between high and low conduction states by switching the light from on to off. In addition, as shown in Fig. 5e the light response of the device remains identical after several tens of switching cycles, showing the excellent stability and reproducibility of the device. Furthermore, the heterojunction photodetector is highly stable in air, showing negligible changes even after storage under ambient conditions for 45 days (see Fig. S3, ESI†).

The effect of the external voltage on device performance was investigated. Fig. 5c and d show the voltage-dependencies of *S*, *D**, *R* and the photocurrent (900 nm light of 100 μW cm^{-2}). It is demonstrated that *S*, *D**, *R* and the photocurrent increase with increasing voltage. At −7 V the *S*, *D** and *R* of the device reach excellent values of 1.47×10^6 cm^2 W^{-1}, 7.4×10^{12} cm Hz$^{1/2}$ W^{-1} and 11.8 A W^{-1}, respectively. Fig. 5g and h show the *S*, *D**, *R* and photocurrent *versus* light power density plots of H:TiO_2 NRAs/SiO_2/Si at a −7 V bias. The photocurrent increases steeply and the increasing light power density leads to saturation of the photocurrent. This is because at a higher light power intensity the increased recombination probability at high concentrations of photo-generated carriers can promote stronger carrier recombination.[25] According to $R = I_p/PA$, $D^{\star} = A^{1/2}R/(2qI_{dark})^{1/2}$ and $S = I_p/I_{dark}P$, *R* and *S* are closely related to I_p and P, and $D^{\star}$ is directly proportional to *R*. I_p fastly approaches saturation with increasing light power density. Therefore, an increase in power density can cause a decrease of *R* or *S* and lead to a reduction

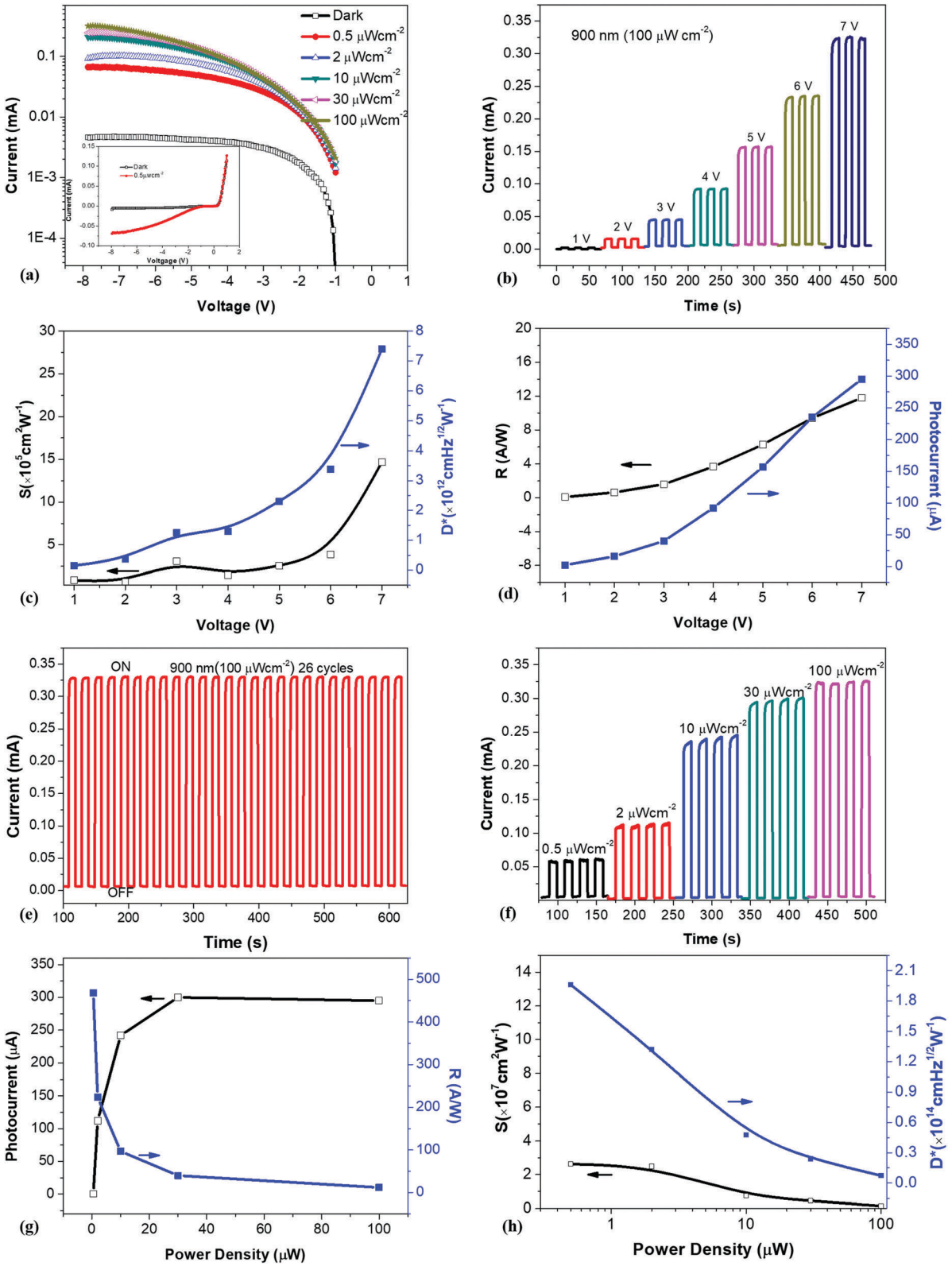

Fig. 5 Comprehensive photo-responsive properties of the H:TiO_2 NRAs/SiO_2/Si heterojunction with H_2-treatment at 350 °C. (a) The logarithmic forms of the *I*–*V* curves of the device measured at RT under darkness and 900 nm light with different light power densities; the inset figure is the *I*–*V* curve of the device under darkness and 900 nm light of 0.5 μW cm^{-2}. (b) Photocurrent *versus* time plots of the H:TiO_2 NRAs/SiO_2/Si heterojunction under 900 nm light of 100 μW cm^{-2} at different voltages. (c and d) *S*, *D**, *R* and photocurrent *versus* voltage plots of the H:TiO_2 NRAs/SiO_2/Si heterojunction under 900 nm light. (e) Photocurrent *versus* time plot of the H:TiO_2 NRAs/SiO_2/Si heterojunction under 900 nm light at −7.0 V for 26 cycles. (f) Photocurrent *versus* time plots of the H:TiO_2 NRAs/SiO_2/Si heterojunction photodetector at −7.0 V under 900 nm light with different light power densities. (g and h) *S*, *D**, *R* and photocurrent *versus* light power density plots of the H:TiO_2 NRAs/SiO_2/Si heterojunction at −7.0 V under 900 nm light.

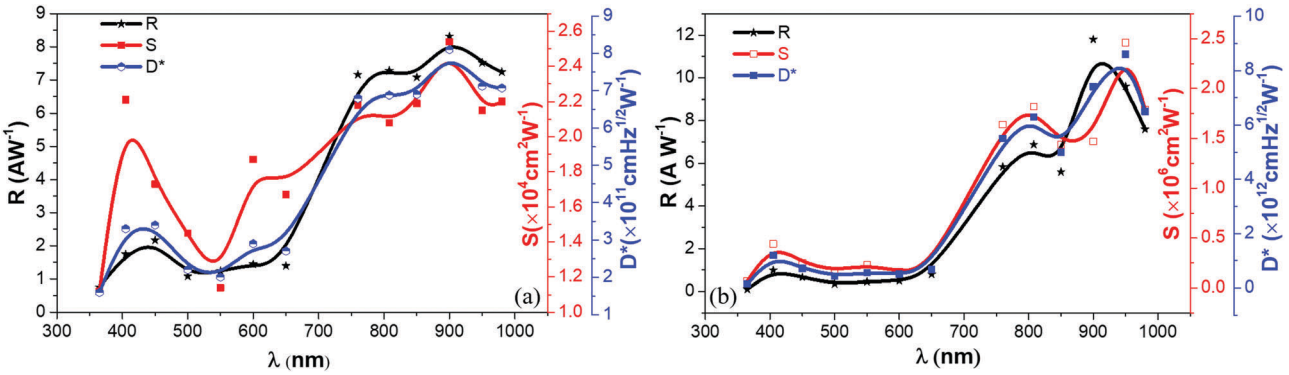

Fig. 6 The *I*–*V* curves of (a) TiO_2 NRAs/SiO_2/Si and (b) H:TiO_2 NRAs/SiO_2/Si with H_2-treatment at 350 °C under darkness and 365–980 nm light (100 μW cm^{-2}).

of D^*. The results also demonstrated that the three figure-of-merits rapidly decreased with increasing incident light power density and reach a minimum value under a light power density of 100 μW cm^{-2}. At a very low light power density of 0.5 μW cm^{-2} the S of the device reaches an excellent value of 2.63 × 10^7 cm^2 W^{-1}, with an outstanding D^* of 1.96 × 10^{14} cm $Hz^{1/2}$ W^{-1} and an ultrahigh R of 468 A W^{-1}.

To assess the broadband detection capability of the H:TiO_2 NRAs/SiO_2/Si heterojunction photodetector, the photo response characteristics of the device in the wavelength range of 365–980 nm were investigated. Fig. S4 (ESI†) shows that the *I*–*V* curves of the H:TiO_2 NRAs/SiO_2/Si heterojunction photodetector show a wide photo-responsive range from UV to NIR light at 100 μW cm^{-2}. The wavelength dependence of R, S and D^* at −7 V bias is as shown in Fig. 6. The R values of H:TiO_2 NRAs/SiO_2/Si increase a little compared to those of the TiO_2 NRAs/SiO_2/Si heterojunctions in the range of UV-NIR light. In addition, according to the defining equations of S and D^*, S and D^* are closely related to both the photocurrent and dark current. As shown in Fig. 6b, compared with those of the TiO_2 NRAs/SiO_2/Si heterojunction, the S and D^* values of H:TiO_2 NRAs/SiO_2/Si are enhanced by 2 orders of magnitude, which should be mainly attributed to the greatly reduced dark current. Overall, the H:TiO_2 NRAs/SiO_2/Si heterojunction shows better photo-responsive properties under UV-NIR light at −7 V and the strongest figure-of-merits are achieved at 760–980 nm.

PDs have been widely used in fields such as optical telecommunication, imaging, *etc.*, for which the high response and recovery time of the detectors is crucial. In this work, the response speed of the H:TiO_2 NRAs/SiO_2/Si heterojunction device was further investigated, as shown in Fig. 7. Fig. 7 shows the time-dependent photo response of the PD measured by periodically turning it on and off in air, demonstrating that the H:TiO_2 NRAs/SiO_2/Si heterojunction also shows excellent stability and reproducible characteristics in other wavelengths of light. Upon illumination, the photocurrent increases to a stable value and then dramatically decreases to its initial value as the light is turned off. Herein, the time taken for the current to change from 10% to 90% of the peak value or *vice versa* is defined as the response time or recovery time, respectively. The schematic diagram of the measurement circuit of the transient response of the H:TiO_2 NRAs/SiO_2/Si

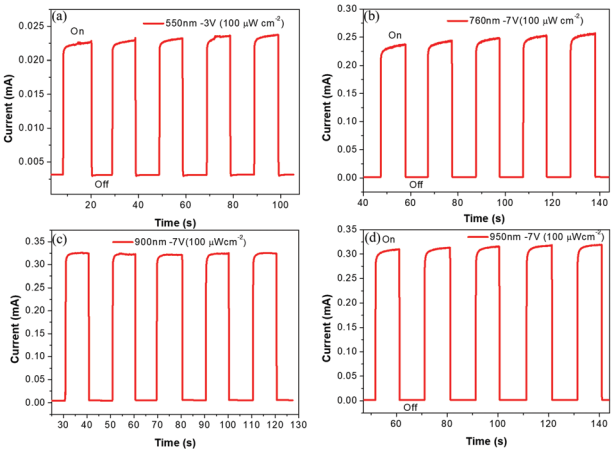

Fig. 7 (a–d) Photocurrent *versus* time plots of H:TiO_2 NRAs/SiO_2/Si with H_2-treatment at 350 °C under different wavelengths of light.

photodetector and the characteristic response times at the rise edge and the fall edge are as shown in Fig. S5a, c and d (ESI†). It is demonstrated that the response and recovery times of H:TiO_2 NRAs/SiO_2/Si heterojunctions are extremely short. Under closer examination, the response and recovery times of the present detector are 3.9 ms and about 3.55 ms, respectively. The response time is closely related to the diffusion and drift times of carriers, which are determined by the absorption layer and depletion layer of heterojunctions, respectively. The drift time is much quicker than the diffusion time. An appropriate reverse voltage can increase the thickness of the depletion layer of heterojunctions and relatively decrease the thickness of the absorption layer, which can reduce the diffusion time of carriers, prolong the carrier lifetime and greatly shorten the transit time of photon-generated carriers. Thus, the drift time has a dominate role. Due to the drift time being much quicker than the diffusion time of carriers, the response and recovery times can be greatly shortened and the photo response speed of the detector is improved.

2.4 Mechanism of the photo response of the H:TiO_2 NRAs/SiO_2/Si heterojunction

In order to deeply understand the photo-responsive mechanism of H:TiO_2 NRAs/SiO_2/Si heterojunctions, the spectral response,

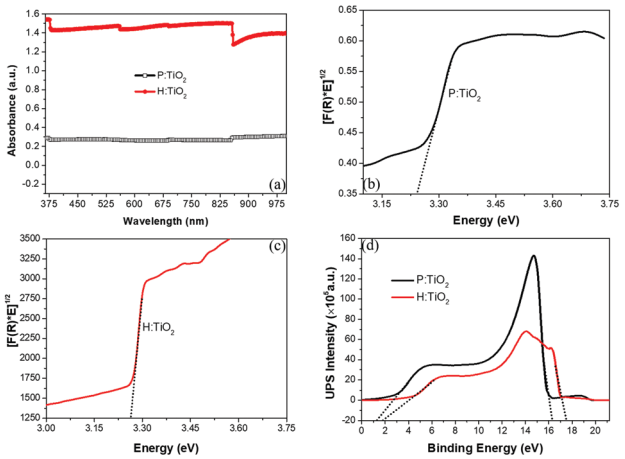

Fig. 8 (a) UV-VIS-NIR spectra of TiO_2 NRAs and H:TiO_2 NRAs/SiO_2/Si with H_2-treatment at 350 °C. (b and c) Determination of the band gaps by plotting $[F(R)E]^{1/2}$ *vs.* energy. (d) shows the initial and cutoff positions of UPS.

UPS and energy band diagram of the heterojunctions should be investigated. Fig. 8a shows that the spectral response of the H:TiO_2 NRAs/SiO_2/Si heterojunctions is stronger in the UV to NIR light range than that of TiO_2 NRAs/SiO_2/Si heterojunctions.[31–34] Absorbance spectroscopy was subsequently performed to acquire the band gaps of the TiO_2 NRAs, as shown in Fig. 8b and c. By performing a Kubelka–Munk transformation,[43] the band gaps of the TiO_2 NRAs and the H:TiO_2 NRAs were determined to be 3.25 eV and 3.27 eV. As shown in Fig. 8d, the UPS spectrum of the TiO_2 NRAs shows a cutoff energy (E_{cutoff}) of 16.375 eV and a HOMO energy (E_{HOMO}) of 2.0 eV, indicating that the work function and electron affinity of the TiO_2 NRAs are 6.2 and 4.95 eV, respectively. For the H:TiO_2 NRAs, the UPS spectrum shows a cutoff energy (E_{cutoff}) of 17.875 eV and a HOMO energy (E_{HOMO}) of 3.0 eV, indicating that the work function and electron affinity of the H:TiO_2 NRAs are 5.075 and 4.81 eV, respectively. The high-magnification TEM image and the XPS O 1s spectrum of the H:TiO_2 nanorods indicate that a core/shell structure TiO_2@$TiO_{2-x}H_x$ structure was formed on the outer surface of the H:TiO_2 nanorods as shown in Fig. 9a which had been demonstrated in former research.[30–32,34] The band structure contributed by the crystalline core is similar to that of the anatase TiO_2 phase, and the $TiO_{2-x}H_x$ shell mainly provides some dispersed Ti^{3+} 3d bands below the CBM and O $2p^6$ bands above the VBM.[30–32,34] The amorphous shell of $TiO_{2-x}H_x$ has no lattice periodicity and breaks the octahedral symmetry of TiO_6 and two tails of the VBM and CBM are formed which can narrow the band gap of TiO_2, resulting in the VIS-NIR light absorption in our samples.[31,32,34] Furthermore, the oxygen vacancies generated in the shell result in a large number of Ti^{3+} ions, and the Fermi level of TiO_{2-x} is shifted to near the CBM. Therefore, the schematic electronic structure of TiO_2 and TiO_2@TiO_{2-x} (denoted as TiO_{2-x}) are proposed in Fig. 9b and c, which have been fully confirmed by other research.[30–32,34] In addition, according to the physics of semiconductors,[44] we can calculate E_F, E_C and E_V of n-Si to be 4.36, 4.05 and 5.16 eV, respectively, as shown in Fig. 9b and c.

As shown in Fig. 9b, according to the schematic energy band diagram the Fermi level of the Si substrate is higher than that of TiO_2. Under darkness when a reverse bias voltage is applied to the heterojunction (n-Si is anodic and TiO_2 is cathodic), the minority carriers (hole carriers in TiO_2 and Si) are conductive carriers and form the dark current. Additionally, under UV-NIR light the number of minority carriers increased obviously compared to the majority carriers. At a reverse voltage, the increased minority carriers participate in drift motion and form the photocurrent.[24] Thus, TiO_2 NRAs/SiO_2/Si heterojunctions demonstrate a photo response to UV-NIR light. As shown in Fig. 9c, after TiO_2 is hydrogenated, due to the energy bands of the TiO_2@$TiO_{2-x}H_x$ structure the Fermi level of H:TiO_2 is raised a lot,[34] the number of majority carriers increases a lot and correspondingly the number of minority carriers decreases greatly. Under darkness the dark current can reduce significantly. On the other hand, under illumination the enhanced UV-NIR spectral response of the H:TiO_2 NRAs makes the photo current further increase. Therefore, the S and D^* of H:TiO_2 NRAs/SiO_2/Si are enhanced remarkably.

In fact, the formation of the photocurrent is closely related to light absorption, carrier transportation and recombination

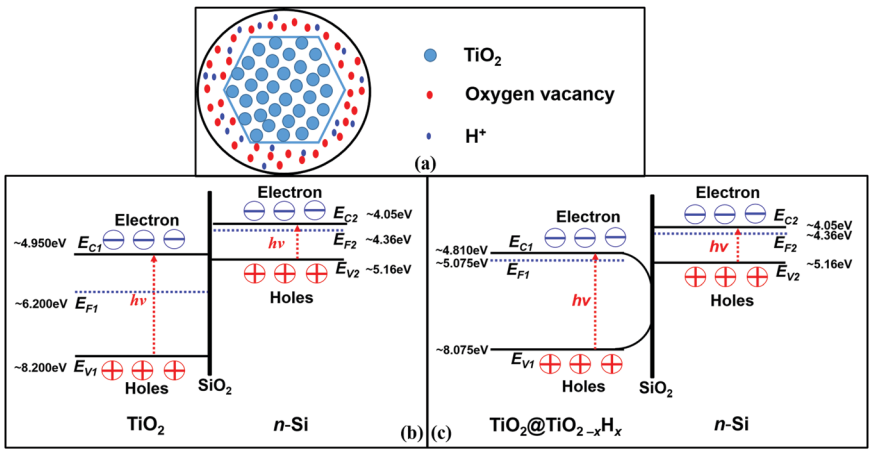

Fig. 9 (a) The structure of TiO_2@$TiO_{2-x}H_x$[32] and the schematic energy band diagram for (b) TiO_2 NRAs/SiO_2/Si and (c) H:TiO_2 NRAs/SiO_2/Si.

Table 1 Comparison among some 1D metal oxide nanostructure or 2D nanomaterial/Si heterojunction photodetectors

Materials and detector	Wavelength	R (A W^{-1})	S (cm^2 W^{-1})	D^* (cm Hz$^{1/2}$ W^{-1})	Rise/fall time	Ref.
H:TiO_2 nanorod arrays/SiO_2/n-Si	365–980 nm	468	2.63×10^7	1.96×10^{14}	50 ms/50 ms	This work
ZnO nanorod arrays/SiO_2/p-Si	300–800 nm	—	9.3×10^3	—	—/—	23
ZnO nanowire arrays/n-Si(100)	350–400 nm	—	1.06	—	—/—	22
TiO_2 nanowires/p-Si	400 W UV-vis	3×10^{-6}	12	—	—/—	45
TiO_2 nanowire arrays/p-Si	432–488 nm	3.5	—	—	2.5 s/2 s	46
TiO_2 nanorod arrays/p-Si	365 nm	—	3.3×10^4	—	18.5 ms/19.1 ms	47
TiO_2 film/TiO_2 nanorod arrays/n-Si	300–600 nm	10^{-6}–10^{-1}	2×10^3	—	—/—	24
Bi_2Se_3/Si	365–1100 nm	24.28	—	4.39×10^{12}	2.5 μs/5.5 μs	25
$SnSe_2$/Si	530 nm	1.1×10^3	1.1×10^6	10^{10}	14.5 ms/8.1 ms	27
WS_2/Si	370–1064 nm	0.7	—	2.7×10^9	4.1 s/4.4 s	18
In_2Te_3/Si	370–1064 nm	44	2.5×10^5	6×10^{12}	15 ms	17
In_2S_3/Si	450–900 nm	137	—	4.74×10^{10}	6 ms/8 ms	28
NiSe/Si	White light	150	—	—	8 s/15 s	26

of photo-generated carriers. Though the spectral response of H:TiO_2 NRAs/SiO_2/Si is enhanced from UV to NIR, the penetration depth of UV-VIS light is shorter and the distance from the photo-generated carriers to the depleted layers of the heterojunction is longer. These factors can increase the recombination probability of photo-generated carriers in transportation processing. Therefore, the photocurrent of the H:TiO_2 NRAs/SiO_2/Si heterojunction is relatively lower under UV-VIS light. The penetration depth of NIR light is greater and the distance from the photo-generated carriers to the depleted layers of the heterojunction is shorter, which makes the recombination probability of the photo-generated carriers decrease greatly. In addition, it had been demonstrated in former research that metal oxide NRAs could guide photons effectively as an antireflective nanostructure in the long-wavelength regions. Therefore, some NIR light can enter the Si layer and can be absorbed.[23] Thus, the photocurrent of the H:TiO_2 NRAs/SiO_2/Si heterojunction is much higher under NIR light than that under UV-VIS light. Accordingly, under NIR light the H:TiO_2 NRAs/SiO_2/Si heterojunction demonstrates a higher photo-responsive performance.

Table 1 summarizes the main device parameters of some 1D metal oxide nanostructure or 2D nanomaterial/Si heterojunction photodetectors obtained under UV-NIR light illumination. Notably, the present device is significantly better than those reported previously for all aspects of performance, achieving an optimal balance among all the critical features. The results are attributed to the following reasons: (i) using surface engineering by H_2-treatment a core/shell structure (TiO_2@$TiO_{2-x}H_x$) was formed on the outer surface of the H:TiO_2 nanorods. Not only was the UV-NIR spectral response of the H:TiO_2 NRAs enhanced, but the Fermi level of H:TiO_2 was also raised a lot and the number of minority carriers decreased greatly. (ii) Combined with the interface effect of the H:TiO_2 NRAs/SiO_2/Si heterojunction, at a reverse voltage the minority carriers are conductive carriers, under darkness the dark current of the H:TiO_2 NRAs/SiO_2/Si heterojunction reduced greatly and under light irradiation the photocurrent further increased. The above two important factors make H:TiO_2 NRAs/SiO_2/Si possess outstanding photo-responsive characteristics. (iii) In addition, it has been demonstrated that the thinner insulating oxide layer (SiO_2) can also improve the response of PDs (the effect of an insulating SiO_2 layer on the photo response of the heterojunction is explained in the ESI I†).

3. Conclusions

In summary, we demonstrated that the H:TiO_2 NRAs/SiO_2/n-Si heterojunction is an excellent broadband photodetector, which shows an ultrahigh photosensitivity and detectivity and an ultrafast response. Notably, the comprehensive properties of the present device are significantly better than those reported previously, achieving an optimal balance among all the critical features. The photodetector possessed a large light responsivity of 468 A W^{-1}, an outstanding detectivity of $\sim 1.96 \times 10^{14}$ cm Hz$^{1/2}$ W^{-1}, an excellent sensitivity of $\sim 2.63 \times 10^7$ cm^2 W^{-1} at 0.5 μW cm^{-2}, and a fast response speed with a rising time of approximately microseconds. More importantly, the H:TiO_2 NRAs/SiO_2/Si heterojunction photodetector was capable of broadband detection ranging from UV to NIR light. The excellent performance of the H:TiO_2 NRAs/SiO_2/Si heterojunction may be mainly attributed to the raised Fermi energy of the TiO_2@$TiO_{2-x}H_x$ core/shell structure and the interface effect between the TiO_2@$TiO_{2-x}H_x$ core/shell structure and Si. This new concept can be extended to other metal oxide nanomaterial/Si heterojunction materials. The high-performance heterojunction photodetector should have important prospects for practical applications, and the integration of such 1D metal oxide nanostructures with a traditional Si semiconductor will open up great opportunities for next-generation optoelectronic devices.

4. Experimental section

4.1 Sample preparation

First, the TiO_2 seed layer was fabricated on the n-type Si(100) substrate (10 mm × 10 mm) with a resistivity of 1–3 Ω cm using a spin-coating method at 8000 rpm for 50 s, wherein the precursor includes ethanol (28.43 ml), TBOT (8.31 ml), distilled water (3.51 ml), acetic acid (9.75 ml) and PVP (2 g) and is stirred under ambient conditions for 30 minutes. Secondly, the spin-coated wafer was then annealed at 800 °C in air under ambient conditions for 2 h and the TiO_2 seed layer was fabricated. The Si

substrate was then washed in ethanol, following which the TiO_2 NRAs were grown using a hydrothermal method. The TiO_2 NRAs grew in an aqueous solution containing hydrochloric acid (30 ml) and a TBOT (1 ml) solution at 160 °C for 2 h. Finally, the TiO_2 NRAs on Si were annealed in a pure hydrogen atmosphere for 60 min at various temperatures in the range 350–500 °C, and developed into H:TiO_2 NRAs.

4.2 Characterization

The fabricated H:TiO_2 NRAs were characterized using a field emission Scanning Electron Microscope (SEM) (JEOL JSM-6500), a Transmission Electron Microscope (TEM) (FEI Tecnai G2 F20), X-ray photoelectron spectroscopy (XPS) (ESCALAB 250Xi), Raman scattering (labRAM HR evolution), X-ray diffraction (XRD) (X'Pert Pro MPD XRD system, CuKα1, λ = 1.5406 Å), an absorption spectrometer (UV3600) and an Ultroviolet Photoelectron Spectrometer (UPS) (ESCALAB 250Xi).

4.3 Device fabrication

A transparent conducting Pd thin film layer was deposited on the surface of the H:TiO_2 NRAs/SiO_2/n-Si heterojunction from a Pd target (Beijing Mountain Technical Development Center, Beijing, China) using DC magnetron sputtering. During the deposition process the argon gas pressure and the deposition power and time were 3 Pa, 40 W and 15 s, respectively. The electrodes on the Pd film surface and the opposite Si surface of the H:TiO_2 NRAs/SiO_2/n-Si broadband detector were made using an In solder.

4.4 Measurement

All the light response of the device was investigated under a CEL-HXF300/CEL-HXUV300 Xenon Light Source. Some single pass filters (band is 10 nm) with 13 wavelengths (365 nm, 405 nm, 450 nm, 500 nm, 550 nm, 600 nm, 650 nm, 760 nm, 808 nm, 850 nm, 900 nm, 950 nm and 980 nm) were used to obtain the light sources. The size of the Pd film was 0.5 cm × 0.5 cm. The diameter of the light was about 10 cm and vertically incident on the sample surface. Therefore, the effective area of the light was 0.5 cm × 0.5 cm. The Xenon Light Source was purchased from Beijing Jinyuan of Science and Technology Co., LTD. The single pass filters were used to obtain monochromatic light of different wavelengths. A FZ400 Light power meter (Beijing Nbets of Science and Technology Co., LTD) was used to measure the light power intensity. The relative humidity in air was 30% and the air pressure was 1.0×10^5 Pa (normal pressure). The *I–V* characteristics of the device were measured using the two-probe method. The two electrodes of each sensor were mounted on a probe holder and connected to a Keithley 2600 source-meter (Keithley Instruments Inc., Cleveland, U.S.) controlled by a computer.

Conflicts of interest

There are no conflicts to declare.

Acknowledgements

This work was supported by the Natural Science Foundation of China (11604390) and the Fundamental Research Funds for the Central Universities (17CX02045).

References

1 D. Xiang, C. Han, Z. Hu, B. Lei, Y. Liu, L. Wang, W. P. Hu and W. Chen, *Small*, 2015, **11**, 4829.
2 I. K. Kim, B. N. Pal, M. Ullah, P. L. Burn, S. C. Lo, P. Meredith and E. B. Namdas, *Adv. Opt. Mater.*, 2015, **3**, 50.
3 R. Dong, C. Bi, Q. Dong, F. Guo, Y. Yuan, Y. Fang, Z. Xiao and J. Huang, *Adv. Opt. Mater.*, 2014, **2**, 549.
4 J. R. Manders, T. H. Lai, Y. An, W. Xu, J. Lee, D. Y. Kim, G. Bosman and F. So, *Adv. Funct. Mater.*, 2014, **24**, 7205.
5 X. Wang, P. Wang, J. Wang, W. Hu, X. Zhou, N. Guo, H. Huang, S. Sun, H. Shen, T. Lin, M. Tang, L. Liao, A. Jiang, J. Sun, X. Meng, X. Chen, W. Lu and J. Chu, *Adv. Mater.*, 2015, **27**, 6575.
6 X. Hu, X. Zhang, L. Liang, J. Bao, S. Li, W. Yang and Y. Xie, *Adv. Funct. Mater.*, 2014, **24**, 7373.
7 K. K. Manga, J. Wang, M. Lin, J. Zhang, M. Nesladek, V. Nalla, W. Ji and K. P. Loh, *Adv. Mater.*, 2012, **24**, 1697.
8 H. Qiao, J. Yuan, Z. Xu, C. Chen, S. Lin, Y. Wang, J. Song, Y. Liu, Q. Khan, H. Y. Hoh, C. X. Pan, S. Li and Q. Bao, *ACS Nano*, 2015, **9**, 1886.
9 H. H. Fang and W. D. Hu, *Adv. Sci.*, 2017, **1**, 1700323.
10 M. L. Lee, J. K. Sheu, Y. K. Su, S. J. Chang, W. C. Lai and G. C. Chi, *IEEE Electron Device Lett.*, 2004, **25**, 593.
11 L. W. Sang, M. Y. Liao, Y. Koide and M. Sumiya, *Appl. Phys. Lett.*, 2011, **99**, 031115.
12 M. L. Sánchez, A. Primo, P. Atienzar, A. Forneli and H. García, *Small*, 2015, **11**, 970.
13 M. L. Lee, P. F. Chi and J. K. Sheu, *Appl. Phys. Lett.*, 2009, **94**, 013512.
14 (*a*) L. Li, P. C. Wu, X. S. Fang, T. Y. Zhai, L. Dai, M. Y. Liao, Y. Koide, H. Q. Wang, Y. Bando and D. Golberg, *Adv. Mater.*, 2010, **22**, 3161; (*b*) L. Li, X. S. Fang, T. Y. Zhai, M. Y. Liao, U. K. Gautam, X. C. Wu, Y. Koide, Y. Bando and D. Golberg, *Adv. Mater.*, 2010, **22**, 4151; (*c*) L. Li, P. S. Lee, C. Y. Yan, T. Y. Zhai, X. S. Fang, M. Y. Liao, Y. Koide, Y. Bando and D. Golberg, *Adv. Mater.*, 2010, **22**, 5145.
15 (*a*) C. Li, Y. Bando, M. Y. Liao, Y. Koide and D. Golberg, *Appl. Phys. Lett.*, 2010, **97**, 161102; (*b*) L. W. Sang, M. Y. Liao, Y. Koide and M. Sumiya, *Appl. Phys. Lett.*, 2011, **98**, 103502.
16 J. D. Yao, Z. Q. Zheng, J. M. Shao and G. W. Yang, *ACS Appl. Mater. Interfaces*, 2015, **7**, 26701.
17 J. D. Yao, J. M. Shao, Y. X. Wang, Z. Zhao and G. W. Yang, *Nanoscale*, 2015, **7**, 12535.
18 J. D. Yao, Z. Q. Zheng, J. M. Shao and G. W. Yang, *Nanoscale*, 2015, **7**, 14974.
19 J. D. Yao, Z. Q. Zheng and G. W. Yang, *J. Mater. Chem. C*, 2016, **4**, 7831.
20 J. D. Yao, Z. Q. Zheng and G. W. Yang, *ACS Appl. Mater. Interfaces*, 2016, **8**, 12915.

21 C. Yang, C. J. Barrelet, F. Capasso and C. M. Lieber, *Nano Lett.*, 2006, **6**, 2929.
22 Z. Guo, D. X. Zhao, Y. C. Liu, D. Z. Shen, J. Y. Zhang and B. H. Li, *Appl. Phys. Lett.*, 2008, **93**, 163501.
23 D. S. Tsai, C. A. Lin, W. C. Lien, H. C. Chang, Y. L. Wang and J. H. He, *ACS Nano*, 2011, **5**, 7748.
24 T. Ji, Q. Liu, R. J. Zou, Y. G. Sun, K. B. Xu, L. W. Sang, M. Y. Liao, Y. S. Koide, L. Yu and J. Q. Hu, *Adv. Funct. Mater.*, 2016, **26**, 1400.
25 H. B. Zhang, X. J. Zhang, C. Liu, S. T. Lee and J. S. Jie, *ACS Nano*, 2016, **10**, 5113.
26 C. Y. Cai, Y. Ma, J. Jeon, F. Huang, F. X. Jia, S. Lai, Z. H. Xu, C. J. Wu, R. Q. Zhao, Y. F. Hao, Y. Q. Chen, S. Lee and M. Wang, *Adv. Mater.*, 2017, **29**, 1606180.
27 X. Zhou, L. Gan, W. M. Tian, Q. Zhang, S. Y. Jin, H. Q. Li, Y. Bando, D. Golberg and T. Y. Zhai, *Adv. Mater.*, 2015, **48**, 8035.
28 W. J. Huang, L. Gan, H. T. Yang, N. Zhou, R. Y. Wang, W. H. Wu, H. Q. Li, Y. Ma, H. B. Zeng and T. Y. Zhai, *Adv. Funct. Mater.*, 2017, **27**, 1702448.
29 X. H. Lu, M. H. Yu, G. M. Wang, T. Zhai, S. L. Xie, Y. C. Ling, Y. X. Tong and Y. Li, *Adv. Mater.*, 2013, **25**, 267.
30 X. H. Lu, G. M. Wang, T. Zhai, M. H. Yu, J. Y. Gan, Y. X. Tong and Y. Li, *Nano Lett.*, 2012, **12**, 1690.
31 Z. Wang, C. Y. Yang, T. Q. Lin, H. Yin, P. Chen, D. Y. Wan, F. F. Xu, F. Q. Huang, J. H. Lin, X. M. Xie and M. H. Jiang, *Adv. Funct. Mater.*, 2013, **23**, 5444.
32 F. Teng, M. Y. Li, C. T. Gao, G. Z. Zhang, P. Zhang, Y. Q. Wang, L. L. Chen and E. Xie, *Appl. Catal., B*, 2014, **148**, 339.
33 Y. Yan, B. Hao, D. Wang, G. Chen, E. Markweg, A. Albrecht and P. Schaaf, *J. Mater. Chem. A*, 2013, **1**, 14507.
34 Z. Wang, C. Y. Yang, T. Q. Lin, H. Yin, P. Chen, D. Y. Wan, F. F. Xu, F. Q. Huang, J. H. Lin, X. M. Xie and M. H. Jiang, *Energy Environ. Sci.*, 2013, **6**, 3007.
35 D. C. Cronemeyer, *Phys. Rev.*, 1959, **113**, 1222.
36 D. C. Cronemeyer and M. A. Gilleo, *Phys. Rev.*, 1951, **82**, 975.
37 W. T. Kim, C. D. Kim and Q. W. Choi, *Phys. Rev. B: Condens. Matter Mater. Phys.*, 1984, **30**, 3625.
38 C. Q. Yu and H. Wang, *Adv. Mater.*, 2010, **22**, 966.
39 C. C. Ling, T. C. Guo, W. B. Lu, Y. Xiong, L. Zhu and Q. Z. Xue, *Nanoscale*, 2017, **9**, 8848.
40 T. Zhaia, S. L. Xie, M. H. Yu, P. P. Fang, C. L. Liang, X. H. Lu and Y. X. Tong, *Nano Energy*, 2014, **8**, 255.
41 X. H. Lu, Y. X. Zeng, M. H. Yu, T. Zhai, C. L. Liang, S. L. Xie, M. S. Balogun and Y. X. Tong, *Adv. Mater.*, 2014, **26**, 3148.
42 G. M. Wang, H. Y. Wang, Y. C. Ling, Y. C. Tang, X. Y. Yang, R. C. Fitzmorris, C. C. Wang, J. Z. Zhang and Y. Li, *Nano Lett.*, 2011, **11**, 3026.
43 L. Li, Z. Chen, Y. Hu, X. W. Wang, T. Zhang, W. Chen and Q. B. Wang, *J. Am. Chem. Soc.*, 2013, **135**, 1213.
44 S. M. Szc, *Physics of Semiconductor Devices*, John Wiley & Sons, New York, 2nd edn, 1981.
45 Z. S. Hosseini, M. Shasti, S. Ramezani Sani and A. Mortezaali, *J. Appl. Phys.*, 2016, **119**, 014503.
46 P. Chinnamuthu, A. Mondal1, J. C. Dhar and N. K. Singh, *Jpn. J. Appl. Phys.*, 2015, **54**, 06FJ01.
47 A. M. Selman and Z. Hassan, *Superlattices Microstruct.*, 2015, **83**, 549.

